Image of local energy anomaly during a heavy rainfall event*

Shuai Yang(杨帅)[1], Qunjie Zuo(左群杰)[1,†], and Shouting Gao(高守亭)[1,2]

[1] *Laboratory of Cloud-Precipitation Physics and Severe Storms (LACS), Institute of Atmospheric Physics, Chinese Academy of Sciences, Beijing* 100029, *China*

[2] *State Key Laboratory of Severe Weather, Chinese Academy of Meteorological Sciences, Beijing* 100081, *China*

(Received 16 June 2017; revised manuscript received 31 July 2017; published online 29 September 2017)

A clear and interesting image of local total energy anomaly (EA) is depicted for a heavy rainfall event in this study. Before the convection development, it exhibits a positive local EA, implying local total energy (TE) experiences heaping up to prepare for the future system development. As the convection grows, it transforms into an opposite spatial modality with negative EA dominant, which means that the local TE is consumed to feed the convection growth in the middle and lower levels. The local total EA has consistent variation regular in intensity with severe weather system evolution. By utilizing the local TE budget equation in variable density fluid, the flux divergence of energy and its components are investigated, which could account for the local TE variation better. To relax the restriction and complexity introduced by identifying sporadic and alternative positive/negative signals of EA, the method taking the absolute-value operator on energy flux divergence is used to further simplify analyses. The derived characteristic signal of absolute EA is clearer and cleaner than before. Thus, the EA could be illustrated based on the active degree of energy supply/consumption in a generalized sense whatever positive or negative anomaly should be it, which could be used easily to identify and even predict the system development for operational application. Note that, although two sets of methodologies are used to define EA herein, they play absolutely different roles in nature throughout the whole context. For example, the taking-perturbation method provides a diagnostic tool to portray a preliminary sketch and to give sufficient necessity of this research, while tendency equation of local TE illuminates more predictive sense and accounts for future local EA related to following system evolution. Therefore, the latter could be a more effective tool to routine usage.

Keywords: local energy anomaly, energy budget equation, heavy rainfall

PACS: 92.70.Gt, 92.70.Cp, 92.60.Qx **DOI:** 10.1088/1674-1056/26/11/119201

1. Introduction

In general, the total energy (TE) of a fluid, including the kinetic, potential and internal energies, is expected to be conserved within an enclosed volume in frictionless, adiabatic fluid.[1,2] However, both gas flow (liquid fluid) and pressure forces will move energy from here to there. Thus, local TE will no longer conserve and produce anomaly somewhat. What anomalous image will TE exhibit as a severe weather system comes?

A complete life cycle for a real severe weather process is usually accompanied by local increase or decrease of TE.[3,4] Local growth of a strong weather system cannot depart from energy supply and consumption. For instance, a local heating by a certain heat source will lead to lifting of warm air, thus positive internal energy anomaly contributes to convection development.[5] Another example, local frontogenesis along with a large temperature gradient caused by the convergence between cold and warm air masses,[6,7] therefore, the "internal energy frontogenesis" strengthens local positive/negative internal energy contrast and further produces more anomaly. The upward motion forced by frontogenesis and local heating rearrange the fluid and change local potential energy and kinetic energy. Jet, another kind of common system associated with severe weather event, produces drastic local kinetic energy anomaly. A warm vortex transits or lingers in one place[8,9] will take on intense potential, internal, and kinetic energies' variations locally. Certainly, the transformations of different kinds of energies happen frequently along with intense development of severe weather system. For example, Orlanski and Katzfey[10] paid some attention to the concept of interaction energy, but they did not seem to deepen their analysis in this direction. Murakami *et al.*[4] gave an example illustrating the atmospheric local energetics and energy interactions between mean and eddy fields, but the theoretical framework is a little complex and their example analyses are performed on the global energy cycle in climate regime. Zhang *et al.*[11] examined the main energy paths and energy cascade processes of the two types of persistent heavy rainfall events over the Yangtze River–Huaihe River Basin, but they placed emphasis on energy interactions. However, as a severe weather system evolves, what a local total EA modality will present is also an interesting question. The system develop-

*Project supported by the Special Scientific Research Fund of the Meteorological Public Welfare of the Ministry of Sciences and Technology, China (Grant Nos. GYHY201406003 and GYHY201406001), the Opening Foundation of the State Key Laboratory of Severe Weather, Chinese Academy of Meteorological Sciences (Grant Nos. 2015LASW-B01 and 2015LASW-A02), and the National Natural Science Foundation of China (Grant Nos. 41375054, 41575064, 91437215, and 41405055).

†Corresponding author. E-mail: zqj@mail.iap.ac.cn

© 2017 Chinese Physical Society and IOP Publishing Ltd

ment expends energy and needs new complementary supply persistently. In such a supply–consumption system, what does the image of local total energy anomaly look like during a severe weather process, such as a heavy rainfall event? Which factors should be responsible for such anomaly? With the aid of TE equation derived in Section 2, the high-resolution numerically simulated output is utilized to visualize the image of local total EA for a heavy mountainous precipitation event in Section 3. Then the possible factors responsible for the evolution of total energy tendency are illuminated. A summary is given in Section 4.

2. Data, model, and methodology

2.1. Data and model description

To better identify more details and local characteristics of the convective-scale precipitation, a high-resolution numerical simulation is necessary to resolve the target region. WRF (weather research and forecasting, V3.7.1) model is configured with two-nested domains with resolutions of 18 km (505×290) and 3 km (655×547). The GFS (global forecast system) reanalysis data with 0.5° resolution and 6-h interval are used as the initial and boundary fields. In this study, we use Yonsei University PBL scheme (YSU). Other physical parameterizations include the Lin scheme, RRTM (rapid radiative transfer model) longwave radiation and Dudhia shortwave radiation schemes,[12] and the Noah LSM.[13,14] The Grell–Devenyi ensemble cumulus scheme[15] is used for the outer domain. The simulation is integrated from 18 UTC 7 July 2013 and lasts for 61 h with the first 6 h as the spin-up time. The model outputs with 10 min interval from the inner D02 domain are utilized to make subsequent analysis. The hourly precipitation data at a 0.1° horizontal resolution observed by automatic weather stations (AWSs) in China merging with the climate prediction center morphing technique (CMORPH) satellite data[16,17] are used to illuminate the observed precipitation pattern during the event.

2.2. Methodology

To explore the distribution modality of the local total EA related to severe weather system development, the TE budget equations both in constant density fluid and in variable density fluid[2] are revisited and discussed again.

2.2.1. The local TE budget equation in a variable density fluid

From the momentum equation in the inviscid and compressible fluid

$$\rho\frac{\mathrm{d}\boldsymbol{v}}{\mathrm{d}t}=-\boldsymbol{\nabla}p-\rho\boldsymbol{\nabla}\Phi, \tag{1}$$

where ρ and p denote density and pressure, $\boldsymbol{v}$ represents the three-dimensional velocity vector, and Φ is the potential for any conservative force per unit mass (e.g., gz for a uniform gravitational field, with symbols g and z representing the gravitational acceleration and geopotential).

By defining the kinetic energy density (or energy per unit volume) $K=\rho\boldsymbol{v}^2/2$, and taking dot product with $\boldsymbol{v}$, equation (1) becomes an equation indicating the change rate of K, yielding

$$\begin{aligned}\frac{1}{2}\rho\frac{\mathrm{d}\boldsymbol{v}^2}{\mathrm{d}t}&=-\boldsymbol{v}\cdot\boldsymbol{\nabla}p-\rho\boldsymbol{v}\cdot\boldsymbol{\nabla}\Phi\\&=-\boldsymbol{\nabla}\cdot(p\boldsymbol{v})+p\boldsymbol{\nabla}\cdot\boldsymbol{v}-\rho\boldsymbol{v}\cdot\boldsymbol{\nabla}\Phi.\end{aligned} \tag{2}$$

For the internal energy ($I=C_vT$, with C_v and T denoting the specific heat of dry air at constant volume and the temperature, respectively) and potential energy (Φ) evolutions at an adiabatic atmosphere, they obey

$$\rho\frac{\mathrm{d}I}{\mathrm{d}t}=-p\boldsymbol{\nabla}\cdot\boldsymbol{v}, \tag{3}$$

$$\rho\frac{\mathrm{d}\Phi}{\mathrm{d}t}=\rho\boldsymbol{v}\cdot\boldsymbol{\nabla}\Phi, \tag{4}$$

respectively. Combining Eqs. (2)–(4), we obtain

$$\rho\frac{\mathrm{d}}{\mathrm{d}t}\left(\frac{1}{2}\boldsymbol{v}^2+I+\Phi\right)=-\boldsymbol{\nabla}\cdot(p\boldsymbol{v}). \tag{5}$$

By utilizing the mass continuity equation, equation (5) is rewritten as

$$\frac{\partial E}{\partial t}+\boldsymbol{\nabla}\cdot[\boldsymbol{v}(E+p)]=0, \tag{6}$$

where $E=\rho(\boldsymbol{v}^2/2+I+\Phi)$ is the total energy (TE, or total energy density, i.e., the TE per unit volume of the fluid).

Equation (6) is the TE equation in the unforced, inviscid and adiabatic, compressible fluid. Note that, the material derivative of E herein is expanded into local tendency and advection, with the latter integrated into the flux form. One important point is that, the flux form in Eq. (6) includes not only the total energy density flux ($\boldsymbol{v}E$) but also an additional term ($\boldsymbol{v}p$). That is to say, as the work is done by the fluid against the pressure force, the energy transfer occurs.

It can be seen that the local change of TE in Eq. (6) is balanced by the flux divergence of $(E+p)$. Thus, a general conservation equation (6) is given, producing a regular and neat form.

2.2.2. Simplify in the constant density fluid

For a constant density (ρ_0) fluid, the momentum equation (1) is simplified as

$$\frac{\mathrm{d}\boldsymbol{v}}{\mathrm{d}t}=-\boldsymbol{\nabla}(\phi+\Phi), \tag{7}$$

where $\phi=p/\rho_0$, the viscosity is also omitted. The mass continuity equation becomes $\boldsymbol{\nabla}\cdot\boldsymbol{v}=0$.

For the advective term on the left-hand side of Eq. (1), using the identity below,

$$(\boldsymbol{v}\cdot\boldsymbol{\nabla})\boldsymbol{v} = -\boldsymbol{v}\times\boldsymbol{\omega} + \boldsymbol{\nabla}(\boldsymbol{v}^2/2). \tag{8}$$

We have

$$\frac{\partial \boldsymbol{v}}{\partial t} + \boldsymbol{\omega}\times\boldsymbol{v} = -\boldsymbol{\nabla}B, \tag{9}$$

where $\boldsymbol{\omega} \equiv \boldsymbol{\nabla}\times\boldsymbol{v}$ and $B = (\phi + \Phi + \boldsymbol{v}^2/2)$ are vorticity and Bernoulli function for constant density fluid, respectively.

Similar to the operation in variable density flow, taking dot product with $\boldsymbol{v}$ and including a constant density ρ_0 to yield

$$\frac{1}{2}\frac{\partial \rho_0 \boldsymbol{v}^2}{\partial t} + \rho_0 \boldsymbol{v}\cdot(\boldsymbol{\omega}\times\boldsymbol{v}) = -\rho_0 \boldsymbol{v}\cdot\boldsymbol{\nabla}B. \tag{10}$$

Obviously, $\rho_0\boldsymbol{v}\cdot(\boldsymbol{\omega}\times\boldsymbol{v})$ equals to zero, thus the kinetic energy (with $K = \rho_0\boldsymbol{v}^2/2$), equation (2) becomes

$$\frac{\partial K}{\partial t} + \boldsymbol{\nabla}\cdot(\rho_0\boldsymbol{v}B) = 0. \tag{11}$$

Considering Φ is time-independent, therefore,

$$\frac{\partial}{\partial t}\left[\rho_0\left(\frac{1}{2}\boldsymbol{v}^2 + \Phi\right)\right] + \boldsymbol{\nabla}\cdot\left[\rho_0\boldsymbol{v}\left(\frac{1}{2}\boldsymbol{v}^2 + \phi + \Phi\right)\right] = 0, \tag{12}$$

or simplified as

$$\frac{\partial E}{\partial t} + \boldsymbol{\nabla}\cdot[\boldsymbol{v}(E+p)] = 0, \tag{13}$$

where $E = K + \rho_0\Phi$ is noted as the TE in constant density flow.

By comparison, equations (13) and (6) are completely identically in form, in which the local budget of total energy is determined by the flux divergence of $(E+p)$ in both constant and variable density fluids.

2.2.3. Difference of local energy budget equation between variable and constant density fluids

2.2.3.1 Difference in form

What differences are there between two expressions? Except that variable density ρ utilized in Eq. (6) is specified as constant density ρ_0 in Eq. (13), the total energy formula E itself utilized in two equations is different in nature. The internal energy vanishes in Eq. (13). Why does this happen? Reverting back to the initial deriving process in constant density fluid, $\boldsymbol{\nabla}\cdot\boldsymbol{v} = 0$ is applied to the mass continuity equation. Therefore, as the connective term between kinetic energy equation (2) and internal energy equation (3), $\boldsymbol{\nabla}\cdot\boldsymbol{v} = 0$ leads to the internal energy change in Eq. (3) disappearing, which indicates that both kinetic energy equation (2) and potential energy equation (4) are sufficient to completely determine the evolution of a system. Just due to this important point, the internal energy tendency is excluded in Eq. (13) for constant density fluid.

2.2.3.2 Difference of the integral of energy in a closed domain

More traditionally, given a spatial domain with rigid boundary condition and without mass flux, it is usually the integral operator but not the local tendency of energy is carried out to investigate the rate of change of TE within the closed volume. From Eqs. (6) and (13), the divergence flux term vanishes by adopting integral over an enclosed volume with rigid boundaries, implying that the TE is conserved for whatever constant or variable density fluids. However, for energy components within the closed domain, energy exchange occurs among kinetic, internal and potential parts in variable density flow, while the case is not the same for the constant density atmosphere. This is because the integral of kinetic energy $\hat{K}$ and gravitational potential energy $\hat{P}$ in constant density fluid are written as

$$\begin{aligned}\frac{\mathrm{d}\hat{K}}{\mathrm{d}t} &\equiv \frac{\mathrm{d}}{\mathrm{d}t}\int_V K\,\mathrm{d}V = -\int_V \boldsymbol{\nabla}\cdot(\rho_0\boldsymbol{v}B)\,\mathrm{d}V \\ &= -\int_S \rho_0 B\boldsymbol{v}\cdot\mathrm{d}S, \end{aligned}\tag{14}$$

$$\hat{P} = \int_V \rho_0 g z\,\mathrm{d}V. \tag{15}$$

According to the divergence theorem, the kinetic energy conservation is satisfied within the closed volume. Note that $\hat{P}$ is a constant and not impacted by a redistribution of flow. Therefore, no exchange presents between kinetic energy and potential energy within a closed constant-density domain, and the kinetic energy itself remains conserved.

2.2.3.3 Difference of usage for time-varying case

The derived TE equations (6) and (13) play roles in two completely different kinds of environmental atmospheres. Generally, the former should have wider application regimes because of its less restriction. However, the latter is simpler to use under some suitable approximation and assumption. For example, the Boussinesq equations are enough to derive TE budget in an incompressible fluid. At this time, the internal energy is divorced from the other components of energy, therefore this term is absent in Eq. (13). Thus, the simplified version of local TE equation (13) exerts its maximal advantage under Boussinesq approximation. In the subsequent analysis, more general usage for time-varying case in variable density fluid will be illustrated as an example.

3. Results

3.1. General description of case study

To investigate the local total EA for a real severe weather event, a heavy precipitation that occurred in western Sichuan near the transition zone between Sichuan Basin and the TP from 8 to 10 July 2013 is generally described. Due to the complex local geography and the special geological structure

over mountainous areas, mudslides broke out accompanying the rainstorm, causing casualties and economic losses. Due to the strong local characteristics, high-resolution numerical simulation is performed to resolve the finer-scale processes.

The circulation backgrounds and synoptic situations are analyzed in Ref. [18]. The precipitation occurred in the western Sichuan basin to the east edge of TP (Fig. 1(a)). The simulated precipitation has similar pattern and magnitude of order with the observation (Fig. 1(b)), except that a little stronger simulated precipitation presents north of 32° N. More local details of precipitations are resolved in Fig. 1(b).

From the evolution of the area-averaged hourly rainfall intensity (Fig. 1(c)), two unambiguous peaks present at 06 UTC on 8 and at 09 UTC on 9 July 2013. Both p.m. peaks accompany twice as large amplitude growths of the vertical motion (Fig. 1(d)). The variation of rainfall intensity is basically consistent with the swing of vertical velocity intensity from 00 UTC 8 to 06 UTC 10 July 2013 (Figs. 1(c) and 1(d)), demonstrating their close correlation. Thus, the initiation and movement of convection may be a key for identifying the convective-scale precipitation development. Based on the simulation and preliminary analyses for the heavy precipitation process with warm vortex,[18] the local total EA related to the convection development and precipitation growth are analyzed by utilizing Eq. (6) from the viewpoint of energy budget.

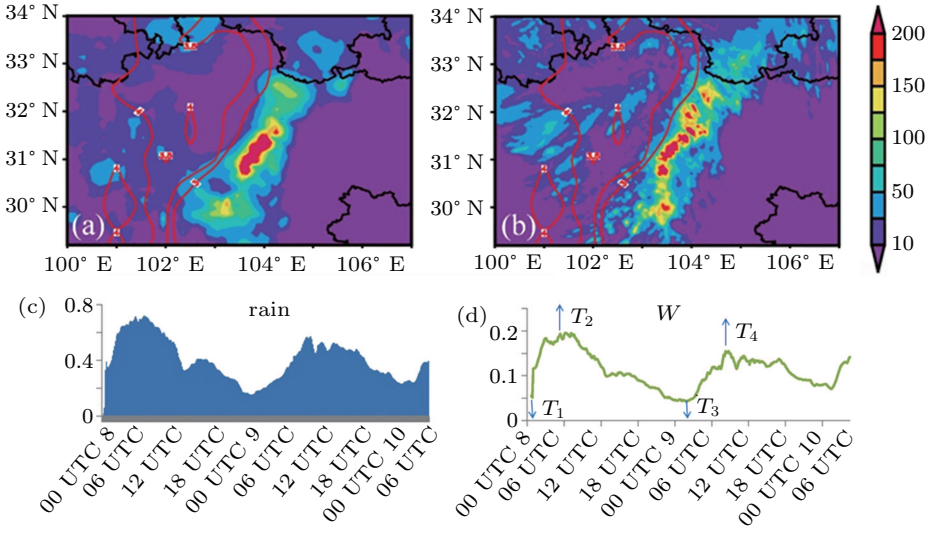


Fig. 1. (a) Observed and (b) simulated total rainfall amount (mm) over western Sichuan Basin from 00 UTC 8 to 06 UTC 10 July 2013. The terrain height above 3 km is outlined; the evolution of area-averaged (c) 10 min precipitation intensity (mm 10 min^{-1}) and (d) vertical motion intensity at 7.58 km level ($\text{m}\cdot\text{s}^{-1}$) from 00 UTC 8 to 06 UTC 10 July 2013. Arrows represent the valley/peak times (T_1, T_3/T_2, T_4) of precipitation and convection evolutions.

3.2. The image of local total EA

Similar diurnal cycles for the intensity evolutions of precipitation and vertical motion emerge on 8 and 9 July 2013. Correspondingly, what anomalies do the energy distributions take on during the evolutions of convection and precipitation evolutions? Figures 2(a)–2(d) show the vertical distributions of TE perturbation from background separation along the strong convection centers, representing the total EA at four typical times (T_1–T_4 shown in Fig. 1(d)).

Note that the extraction of perturbation refers to Refs. [19] and [20], in which the background field of TE is not simple time average or spatial mean as usual, but defined as to vary both with space and time. In an easy-to-understand mathematical language, for the TE, $E(x,y,z,t)$ as an instance in this study, its spatial mean over a fixed area (e.g., domain 2 herein) is $\bar{E}_A(z,t)$ and its time average over a time window (the whole simulation period except for the first 6 h as spin-up time) is $\bar{E}_t(x,y,z)$. Thus, $\bar{E}_{At}(z)$, the time average of $\bar{E}_A(z,t)$, is just a function of z. If ΔE is defined as $\Delta E(z,t) = \bar{E}_A(z,t) - \bar{E}_{At}(z)$, the deviation from its time average can account for the gradual increase/decrease of the areal-mean TE with time as the system moves. Then the background and perturbation are computed as $E_0(x,y,z,t) = \bar{E}_t(x,y,z) + \Delta E(z,t)$ and $E'(x,y,z,t) = E(x,y,z,t) - E_0(x,y,z,t)$. Therefore, E_0 varies with both location and time, containing the averaged spatial pattern plus the change in its mean value with time. The perturbation TE sufficiently embodies the energy anomaly within the simulated domain during the overall period of severe weather process, and also considering the variation of background field with system evolution.

Before system development, there is vast convergence of sinking motions (shaded), except for a weak updraft between 103° E and 104° E below 5 km level (Fig. 2(a)). The positive EA (contour) with the value $> 100\ \text{kg}\cdot\text{m}^{-1}\cdot\text{s}^{-2}$ dominates east of 103° E in middle-lower troposphere at time T_1 (or noted as Valley1 time, below are the same), implying local energy accumulation. Above 14 km level, negative EA spreads widely from west to east.

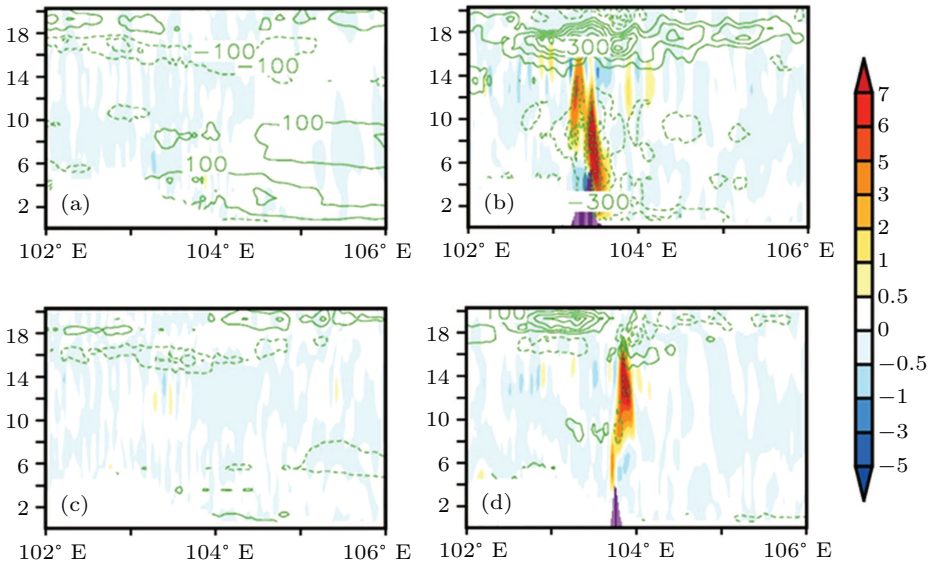


Fig. 2. The vertical distributions of total energy perturbation from background separation along the strong convection centers (31.2° N herein), representing the total energy anomaly (contour, kg·m^{-1}·s^{-2}). The vertical motion is superposed with shaded (m·s^{-1}) (a) at valley 1 time; (b) at peak 1 time; (c) at valley 2 time; (d) at peak 2 time.

At time T_2 (or peak 1, Fig. 2(b)), a pair of strong convection cells (>7 m/s) stretch upwards, with two centers at (7 km, 103.5° E) and (11 km, 103.2° E), respectively. The weak sinking motion is located at both flanks of the strong updrafts. The precipitation occurs between two updrafts. The negative energy perturbation less than 300 kg·m^{-1}·s^{-2} dominates the regions between 103°–104° E, superposing strong convection, which means local energy consumption to feed the convection growth. Different from the case at time T_1, upper-level positive TE anomaly, rolling out a long way off the center of strong convection, is coupled with the lower-level negative TE anomaly.

On 9th July 2013, another diurnal cycle with one wave peak and one valley of system evolution (Figs. 1(c) and 1(d)) occurs. Correspondingly, a similar positive-negative coupled EA presents at time T_3 (or valley 2, Fig. 2(c)), similar to that at valley 1 time except with a little weak intensity, signifying the re-accumulation of local energy. At time T_4 (or peak 2, Fig. 2(d)), the left-side convection in Fig. 2(b) disappears and is replaced by a wide region of sinking motion (Fig. 2(d)). The leading-side convection and related precipitation propagating to 103.7° E, overlaid by negative EA, is weakened and stretched upwards to mid-higher level. The distribution modality also presents lower-level negative and upper-level positive EA above convection and precipitation, with similar pattern but smaller strength relative to the case at peak 1 (Fig. 2(b)).

From above analyses, a clear image of local total EA is portrayed. At the first valley time, local TE experiences heap up to prepare for the future system development. Then the peak time local energy is consumed to feed the convection growth. Till another valley time of the second diurnal cycle, local energy goes through piling up again. It is stored to supply for the convection re-development of the second time. Undoubtedly, the local energy undergoes great expenditure once again. This is the image of local energy anomaly below the height where updraft could touch upwards. Continuing to extend upwards, an opposite-phase EA spreads above 14 km level, just like a wide cloud anvil in appearance (Fig. 2(b)). Therefore, the local total EA presents lower-level negative and upper-level positive modality at peak time while it transforms into an opposite pattern at valley time, with consistent variation regular in intensity with system evolution.

3.3. The tendency equation of local total EA

Since the local TE shows some anomaly and exhibits a meaningful spatial image during the evolution of severe weather, the possible internal mechanism responsible for the local EA variation is necessary to be revealed further by utilizing Eq. (6). To avoid the inaccuracy introduced by time derivative, the flux divergence term in Eq. (6) is computed based on high-frequency model output, 10-minutes intervals herein, to give attribution to local TE change during the severe weather event.

Reverting back to Eq. (6), if the divergence flux term is moved to the right-hand side of this formula, the backhander minus sign is attached thus it becomes $-\nabla\cdot[\boldsymbol{v}(E+p)]$. This new form is composed of four terms, $-\boldsymbol{v}\cdot\nabla E$, $-\boldsymbol{v}\cdot\nabla p$, $-E\nabla\cdot\boldsymbol{v}$, $-p\nabla\cdot\boldsymbol{v}$, denoting E and p advections effects for the former two terms and three-dimensional divergences of E and p for the latter two. It is the coaction among them that produces local total EA. Since similar diurnal cycles for the system evolution on 8 and 9 July 2013, the cases at valley 1 (left column, Figs. 3(a), 3(c), 3(e), 3(g), and 3(i)) and peak 1 (Figs. 3(b), 3(d), 3(f), 3(h), and 3(j)) times are used to make analyses as examples. At valley 1 time, positive advections

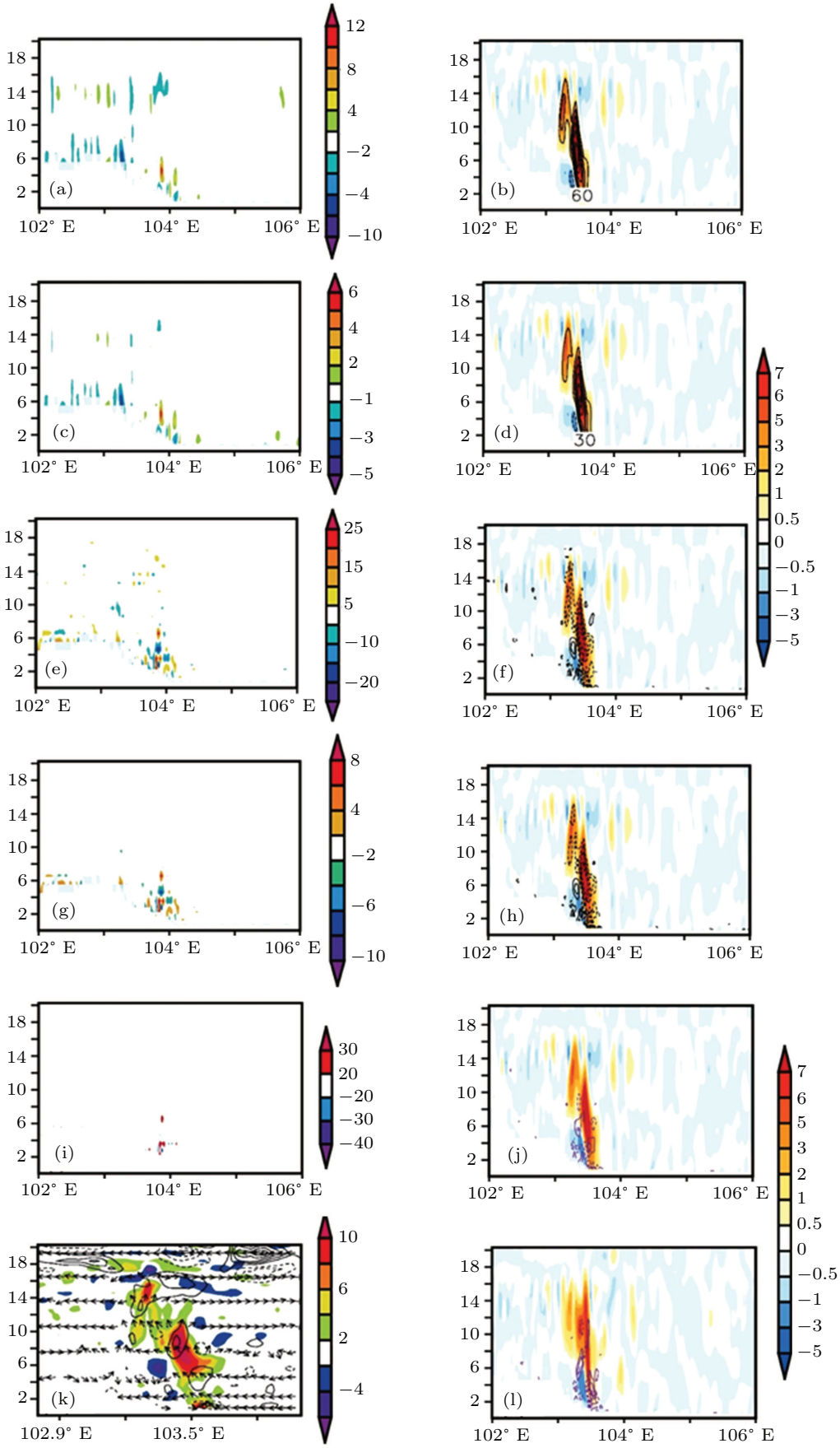


Fig. 3. The zonal-vertical cross sections of energy divergence flux and its components in Eq. (6) along 31.2° N at valley 1 time (shaded, kg·m^{-1}·s^{-2}, (a), (c), (e), (g), and (i)) and peak 1 time (contour, kg·m^{-1}·s^{-2}, superposed with vertical motion, m·s^{-1}, (b), (d), (f), (h), (j)). (a) and (b) $-\boldsymbol{v}\cdot\nabla E$; (c) and (d) $-\boldsymbol{v}\cdot\nabla p$; (e) and (f) $-E\nabla\cdot\boldsymbol{v}$; (g) and (h) $-p\nabla\cdot\boldsymbol{v}$; (i) and (j)$-\nabla\cdot[\boldsymbol{v}(E+p)]$. (k) The three-dimensional divergence (shaded, 10^{-4} s^{-1}), temperature perturbation (contour, K), and wind vector (m·s^{-1}). (l) The same as that in panel (j), except at 10 min-later time.

(shaded in Figs. 3(a) and 3(c)) and the alternatively distributed convergence/divergence of E and p (shaded in Figs. 3(e) and 3(g)) clearly present near 103.5° E in the lower troposphere. Their interaction leads to weak positive EA (Fig. 3(i)), implying energy reservation before the system development. At peak 1 time, positive advections of E and p (contour in Figs. 3(b) and 3(d), with solid line representing positive advection) and divergence of E and p (contour, dashed line denoting divergence) overlaid the strong updraft (shaded). Thus, advection and divergence effects have clear task assignments, respectively. One is in charge of supplying energy for the local convection growth, the other expends local energy. After offsetting each other between positive advections and divergences of E and p because of their opposite signs, the remainder parts account for the graphic distribution of local total EA shown in Fig. 3(j). There are scattered negative energy divergence fluxes within updrafts at peak 1 time. At the following time (i.e., 10 min later, Fig. 3(l)), the left-side branch of convective cells is weakened and the convective systems propagate eastwards, there are always fragmented positive divergence fluxes of energy dispersed at the leading side of system propagation.

To elucidate the relative contribution of several components to total divergence flux of energy, Table 1 quantifies their intensity variations at valley and peak times as illustrations, respectively. From Table 1, two advection terms take positive values within updrafts (in bold font) before and during the simulated period. As for two divergence terms, the sporadic positive and negative signals are alternatively and irregularly presented at valley times, but keep strong negative divergence at peak times within convective regions (Fig. 3), with $-E\nabla\cdot\boldsymbol{v}$ having the largest contribution to $-\nabla\cdot[\boldsymbol{v}(E+p)]$. To a large extent, the divergence term of E and p are determined in modality by the three-dimensional divergence (shaded in Fig. 3(k)), which closely depends on the patterns of related thermal (contour, showing the temperature perturbation) and dynamic (wind vector) meteorological elements. It should also be noted that these components are larger in intensities at peak 1 time than that at peak 2 time, which is consistent with the system evolution (Figs. 1(c) and 1(d)). Relative to the valley time, two peak times accompany with more energy consumption and supply, producing more EA.

Table 1. The intensity variations (kg·m^{-1}·s^{-2}) and the relative contribution of several components to total divergence flux of energy in Eq. (6) at valley and peak times (shown in Fig. 1(d)) as illustrations, respectively. The characteristic maximal/minimal values within updrafts are denoted in bold font.

	Valley 1	Peak 1	Valley 2	Peak 2
$-\boldsymbol{v}\cdot\nabla E$	−10–**12**	−20–**120**	−5–**6**	−2–**70**
$-\boldsymbol{v}\cdot\nabla p$	−5–**6**	−10–**60**	−3–**3.5**	−3–**24**
$-E\nabla\cdot\boldsymbol{v}$	−25–25	**−240**–60	−25–20	**−140**–80
$-p\nabla\cdot\boldsymbol{v}$	−10–8	**−90**–20	−6–8	**−50**–30
$-\nabla\cdot[\boldsymbol{v}(E+p)]$	−40–30	−300–150	−30–25	−180–90

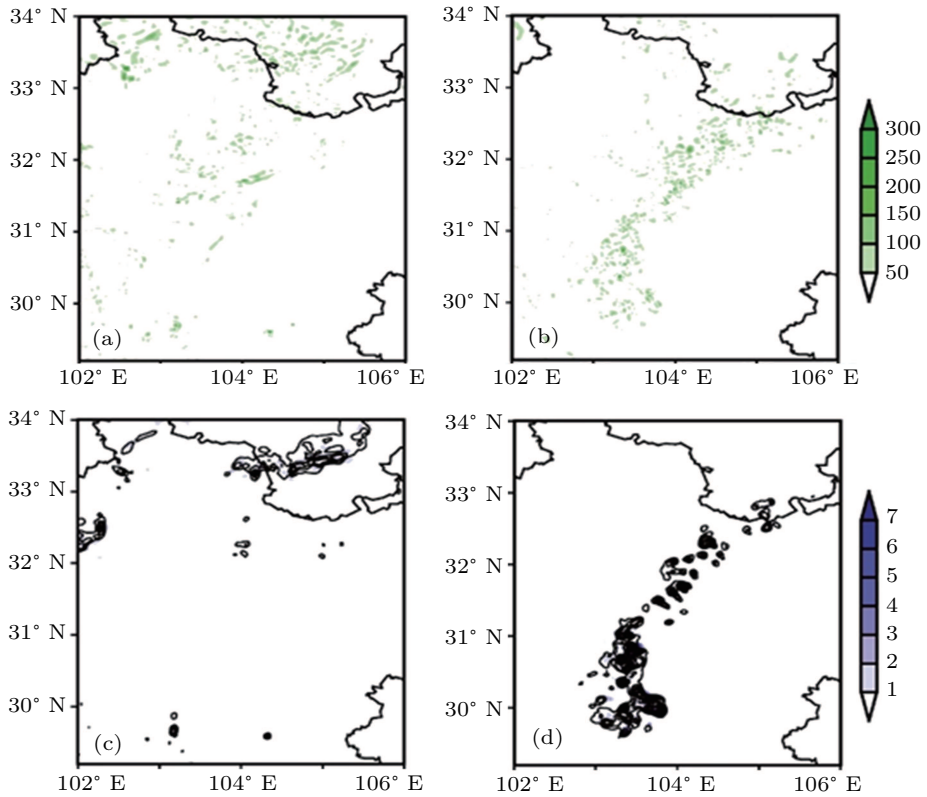


Fig. 4. (a) and (b) The horizontal distributions of absolute total energy anomaly (shaded, kg·m^{-1}·s^{-2}), (c)–(d) along with the associated precipitation (contour, mm) and vertical velocity (with the value >1 m·s^{-1} shaded) at valley 1 ((a) and (c)) and peak 1 ((b) and (d)) times.

From above analyses, the irregularly positive–negative alternative signals of energy flux divergence bring more complexity for operational prediction. To simplify, the method of taking the absolute value of energy flux divergence is adopted herein. Thus, EA is given in a generalized sense whatever positive anomaly or negative one should be it, termed as absolute EA. After the absolute-value operator on energy flux divergence, it is convenient to routine application for forecasters to track the system evolution by visualizing the absolute EA. Figure 4 examines the horizontal distributions of absolute EA (Figs. 4(a) and 4(b)), along with the associated precipitation and convection (Figs. 4(c) and 4(d)) at valley 1 and peak 1 times. From Figs. 4(a) and 4(c), precipitation is absent south of 32° N, but the energy begins gathering in the future rainy region. As the precipitation increases and convection bursts (Fig. 4(d)), there are clear EA signals near the rain belt, which indicates that the local energy activity is frequent and the supply/consumption is very active.

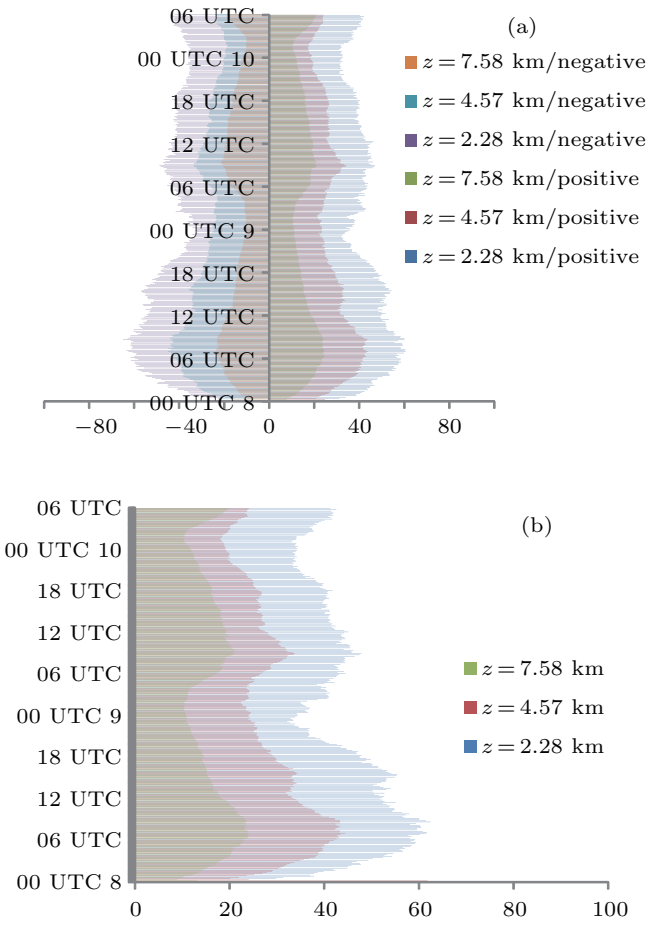


Fig. 5. Evolutions of domain-averaged (a) positive/negative total energy anomaly (kg·m^{-1}·s^{-2}) and (b) its absolute value (kg·m^{-1}·s^{-2}) at different height levels.

Figure 5 shows the evolutions of both total EA and absolute EA. After region-averaged operation, the intensity of (absolute) energy anomaly (Figs. 5(a) and 5(b)) is weakened relative to that at peak time (Figs. 3(j) and 4(b)), but the two diurnal cycles with the first stronger (> 60 kg·m^{-1}·s^{-2}) and the second weaker (about 45 kg·m^{-1}·s^{-2}) are still unambiguously identified. In Fig. 5(a), positive and negative energy anomalies are roughly equivalent in magnitude but with a little stronger positive/negative value at valley/peak time by a subtler survey. The absolute EA (Fig. 5(b)) is more succinctly indicative of the system evolution (Figs. 1(c) and 1(d)), whatever in graphic visualization or from concise concept itself.

4. Summary

By utilizing a severe weather process, e.g., a heavy rainfall event in this study, the image of local total EA is portrayed in detail. What factors should be responsible for such anomaly is investigated based on the local TE budget equation in variable density fluid. Above analyses are summarized as follows.

1) Comparing the local TE budget equation in variable density fluid with its simplified version in constant density flow, it is found that the internal energy vanishes for the latter in form. After integral of energy in a closed domain, the TE conservation is satisfied because the divergence flux term disappears. However, for energy components within the closed domain, energy exchange occurs among kinetic, internal and potential parts in variable density flow, while no exchange presents within a closed constant-density domain, and the kinetic energy itself remains conserved. Generally speaking, the simplified version of local TE equation (13) exerts its maximal advantage under a certain assumption (e.g., Boussinesq approximation). However, the more general usage for time-varying case in variable density fluid should have wider application regimes because of its less restriction.

2) A clear image of local total EA is depicted. The local total energy anomaly based on taking perturbation method[19,20] presents lower-level negative and upper-level positive coupled modality at peak time while it transforms into an opposite pattern at valley time, with consistent variation regular in intensity with system evolution. The distribution pattern implying that, local total energy experiences heaping up to prepare for the future system development at valley time, then the peak time local energy is consumed to feed the convection growth in the middle and lower levels.

3) By utilizing the local TE equation (6), which factors should be responsible for the local EA are investigated. To avoid the inaccuracy introduced by time derivative, the flux divergence term in Eq. (6) and its components are computed to explain local TE change. It shows that two positive advection effects remain during the overall process, implying lasting supply of energy. As for two divergence terms, the scattered positive/negative signals are alternatively and irregularly presented at valley times, but keep strong negative divergence at peak times within convective regions, with $-E\nabla\cdot\boldsymbol{v}$ having the largest contribution to $-\nabla\cdot[\boldsymbol{v}(E+p)]$. It should also be

noted that, the divergence flux term and its components evolve in intensity consistently with the system development.

4) After the absolute-value operator on energy flux divergence, the characteristic signal of absolute EA is clearer and cleaner than before. Thus, the energy anomaly could be illustrated based on the active degree of energy supply/consumption in a generalized sense whatever positive anomaly or negative one should be it, which could be used easily to identify and even predict the system development for operational application.

Note that, perturbation field of E is used to give the image of local total EA in Subsection 3.2. However, the local tendency of E is assumed as the anomaly in Subsection 3.3, because the difference of E between two continuous times removes and cancels the effect of background field in certain degree. They are not completely identical in distribution pattern and in magnitude, determined by the evaluation method of background and perturbation fields specified in Subsection 3.2. Because of longer time windows selected based on Wang *et al.*,[19,20] more mass accumulation above updrafts in upper level causes high pressure and positive potential energy perturbation, which could account for the widely-spreading positive TE anomaly and larger intensity shown in Fig. 2(b) but not in Fig. 3(j). In nature, the taking-perturbation method provides a diagnostic tool to portray a preliminary sketch and to give sufficient necessity of this research, while tendency equation of local total energy indicates more predictive sense and accounts for future local energy anomaly related to further system evolution. Therefore, the latter will be a more effective tool to operational application.

References

[1] Lorenz E N 1955 *Tellus* **7** 157

[2] Vallis G K 2006 *Atmospheric and Oceanic Fluid Dynamics: Fundamentals and Large-scale Circulation* (Cambridge: Cambridge University Press) p. 40

[3] Murakami S 2011 *J. Atmos. Sci.* **68** 760

[4] Murakami S, Ohgaito R and Abe-Ouchi A 2011 *J. Atmos. Sci.* **68** 533

[5] Li Q, Yang S, Cui X P and Gao S T 2017 *Atmos. Oceanic. Sci. Lett.* **10** 235

[6] Yang S, Gao S T and Lu C G 2014 *Adv. Atmos. Sci.* **31** 1065

[7] Yang S, Gao S T and Lu C G 2015 *Adv. Atmos. Sci.* **32** 635

[8] Yang S and Gao S T 2014 *Chin. Phys. B* **23** 119201

[9] Yang S, Zuo Q J and Gao S T 2017 *Chin. Phys. B* **26** 089201

[10] Orlanski I and Katzfey J 1991 *J. Atmos. Sci.* **48** 1972

[11] Zhang Y C, Sun J H and Fu S M 2017 *Adv. Atmos. Sci.* **34** 129

[12] Dudhia J 1989 *J. Atmos. Sci.* **46** 3077

[13] Chen F and Dudhia J 2001 *Mon. Wea. Rev.* **129** 569

[14] Ek M B, Mitchell K E, Lin Y, Rogers E, Grunmann P, Koren V, Gayno G and Tarpley J D 2003 *J. Geophys. Res.* **108** 8851

[15] Grell G A and Devenyi D 2002 *Geophys. Res. Lett.* **29** 1693

[16] Shen Y, Xiong A Y and Wang Y 2010 *J. Geophys. Res.* **115** D02114

[17] Pan Y, Shen Y, Yu J J and Zhao P 2012 *Acta Meteor. Sin.* **70** 1381

[18] Huang Y J 2016 *The Characteristics of Moisture Sources of Torrential Events and the Surface Rainfall Processes in Sichuan Basin* (Doctoral Thesis) p. 90

[19] Wang C C, Kuo H C, Johnson R H, Lee C Y, Huang S Y and Chen Y H 2015 *Atmos. Chem. Phys.* **15** 11097

[20] Wang C C, Chiou B K, Chen G T J, Kuo H C and Liu C H 2016 *Atmos. Chem. Phys.* **16** 12359